

**One- and two-magnon excitations in the antiferromagnet PbFeBO<sub>4</sub>**M. A. Prosnikov \**High Field Magnet Laboratory (HFML-EMFL), Radboud University, Toernooiveld 7, 6525 ED Nijmegen, Netherlands and Institute for Molecules and Materials, Radboud University, Heyendaalseweg 135, 6525 AJ Nijmegen, Netherlands*

(Received 29 October 2020; revised 16 March 2021; accepted 17 March 2021; published 29 March 2021)

The linear spin-wave theory study of PbFeBO<sub>4</sub> spin dynamics is presented. It is shown that the magnetic excitations previously observed in Raman scattering experiments below Néel temperature are optical magnon and two-magnon modes. Based on the magnon energy, two-magnon band line shape, and the Weiss temperature, the consistent set of the exchange coupling constants up to the third-nearest neighbor is derived and compared with the results of *ab initio* calculations available in the literature. The small deviation of the observed two-magnon band from the one-magnon density of states suggests a surprisingly negligible role of magnon-magnon interactions.

DOI: [10.1103/PhysRevB.103.094443](https://doi.org/10.1103/PhysRevB.103.094443)**I. INTRODUCTION**

The promising field of antiferromagnetic spintronics [1–4] constantly demands the discovery of new functional materials with specified properties and the development of reliable theoretical models. Some potential material candidates manifest intrinsic coupling of different subsystems such as magnetic, orbital, electronic, and lattice, allowing for additional degrees of freedom to control spin excitations [5–7].

The PbMBO<sub>4</sub> ( $M = \text{Cr, Mn, Fe}$ ) family of compounds belongs to the sillimanite group [8], where the presence of the stereochemically active Pb<sup>2+</sup> cations leads to the reduction of the connectivity between magnetic ions, resulting in the unique topology of the exchange structure [9]. Moreover, the types of magnetic ions drastically affect magnetic properties, such as magnetic structures, critical temperatures, and dispersion of the magnetic excitations without change of crystal symmetry. Notably, PbMnBO<sub>4</sub> is an extremely rare example of insulating ferromagnets [10,11], while others (PbFeBO<sub>4</sub> and PbCrBO<sub>4</sub>) are known to be antiferromagnets [10]. There are a few predicted compounds with other 3*d* ions, PbMBO<sub>4</sub> ( $M = \text{Ti, V, Co}$ ) [12], which are yet to be synthesized.

In this family, PbFeBO<sub>4</sub> ( $S = 5/2$ ) exhibits the highest transition temperature of  $T_N = 114$  K, and shows anisotropic and negative thermal expansion observed with X-ray and neutron diffraction [13], and anomalies in the vicinity of  $T_N$  in both dielectric susceptibility [14] and phonon energies [15] indicating coupling between magnetic and lattice subsystems. Magnetostatic and dielectric properties of PbFeBO<sub>4</sub> and PbMnBO<sub>4</sub> were studied in detail in Refs. [11,14]. There are a number of *ab initio* calculations [12,16–18] dedicated to the determination of the exchange constants. Simultaneously, the reliable determination of the exchange constants is the crucial step in understanding both the static and dynamical properties of the material and its further potential for applications.

In this paper, we report on the linear spin-wave theory calculations allowing us to derive a closed-form magnon dispersion relation for PbFeBO<sub>4</sub> (and equivalent compounds), calculation of the two-magnon (2M) band line shape, and ground state phase diagram for exchange couplings up to the third nearest neighbor. The set of the exchange constants ( $J_0, J_1, J_2$ ) is proposed based on the experimentally observed energy of the optical branch and shape of the 2M band [15], consistent with all experimental observations to date, including the Weiss temperature [14]. It is shown that both interchain couplings ( $J_1, J_2$ ) are crucial to capture the peculiarities of the spin dynamics. Their values, considering coordination numbers, are comparable with the intrachain one ( $J_0$ ) classifying PbFeBO<sub>4</sub> as a three-dimensional (3D) Heisenberg antiferromagnet. The symmetry-allowed Dzyaloshinskii-Moriya interaction (DMI) on the  $J_0$  path could explain the magnetic susceptibility anomaly [14] in the absence of a weak ferromagnetic moment and could be directly observed by the zero-field splitting of the acoustical magnon branch. The estimated energy range of magnetic excitations for PbCrBO<sub>4</sub> is briefly discussed at the end.

**II. RESULTS AND DISCUSSION**

PbFeBO<sub>4</sub> has orthorhombic crystal structure and belongs to space group  $Pnma$  (No. 62,  $Z = 4$ ). The structure consists of [FeO<sub>6</sub>] octahedra sharing a common edge resulting in octahedral chains running along the  $b$  axis. These chains are connected by rigid [BO<sub>3</sub>] groups and lone-pair Pb<sup>2+</sup> ions, as shown in Fig. 1.

Below  $T_N = 114$  K, PbFeBO<sub>4</sub> undergoes a paramagnet-to-antiferromagnet phase transition, with the resulting propagation vector of the magnetic structure  $\mathbf{k} = (0, 0, 0)$  according to the powder neutron diffraction measurements [10]. The resulting magnetic structure can be described as ferromagnetically coupled antiferromagnetic chains (see Fig. 1).

Based on exchange interactions up to the third nearest neighbor, the  $\mathbf{k} = (0, 0, 0)$  ground state phase diagram is calculated through energy minimization [19] and shown in

\*yotungh@gmail.com

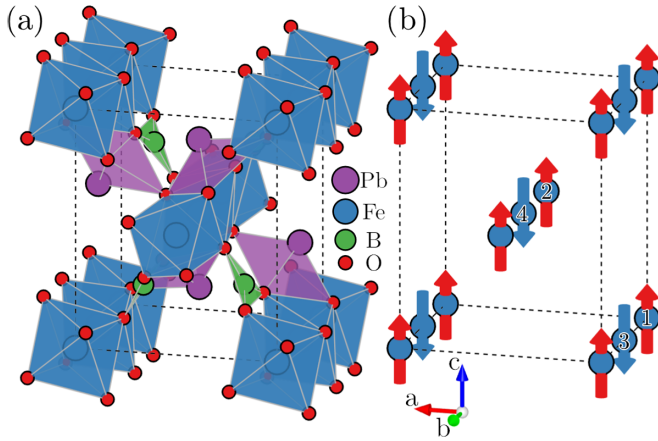


FIG. 1. (a) Crystal structure of  $\text{PbFeBO}_4$  in polyhedral representation. (b) Magnetic structure of  $\text{PbFeBO}_4$  according to Ref. [10]; only  $\text{Fe}^{3+}$  ions are shown, and numbers show indexes of nonequivalent moments in the cell (see Table I).

Fig. 2. Two cases of antiferromagnetic (AFM) and ferromagnetic (FM) intrachain interactions were considered, and it is shown that all possible  $\mathbf{k} = (0, 0, 0)$  magnetic structures could be realized in both cases; however, taking into account the dominant role of  $J_0$  the most probable structures are AFM2 and AFM1 for  $J_0 > 0$  and FM and AFM3 for  $J_0 < 0$ , respectively.

The system is described with the following Hamiltonian based on isotropic exchange interactions and single-ion anisotropy (SIA) terms:

$$\mathcal{H} = \sum_{\langle i,j \rangle} J_0 \mathbf{S}_i \mathbf{S}_j + \sum_{\langle\langle i,j \rangle\rangle} J_1 \mathbf{S}_i \mathbf{S}_j + \sum_{\langle\langle\langle i,j \rangle\rangle\rangle} J_2 \mathbf{S}_i \mathbf{S}_j + \sum_i D (S_i^z)^2, \quad (1)$$

TABLE I.  $\text{Fe}^{3+}$  magnetic ion positions in lattice units and  $\mathbf{u}_j$  and  $\mathbf{v}_j$  vectors defining transformation of spins in the rotating frame.

$j$	$\mathbf{t}_j$	$\mathbf{u}_j$	$\mathbf{v}_j$
1	(0, 0, 0)	(1, $i$ , 0)	(0, 0, 1)
2	(1/2, 0, 1/2)	(1, $i$ , 0)	(0, 0, 1)
3	(0, 1/2, 0)	(1, $-i$ , 0)	(0, 0, -1)
4	(1/2, 1/2, 1/2)	(1, $-i$ , 0)	(0, 0, -1)

where  $\mathbf{S}$  is the spin operator, and  $J_0, \dots, J_2$  stand for superexchange constants corresponding to paths shown in Fig. 2.  $J > 0$  corresponds to AFM exchange.

The general idea of the linear spin-wave theory solution is based, first, on local transformation of classical spin vectors to the ferromagnetic state along the  $z$  axis (coinciding with the  $c$  axis of the crystal) [20–23]. With the change of the rotating frame a new set of spin operators is defined, and with the second transformation every moment in the cell is rotated to form a ferromagnetic state:

$$\begin{aligned} \mathbf{S}_{nj} &= R_n \mathbf{S}'_{nj}, \\ \mathbf{S}'_{nj} &= R'_j \mathbf{S}''_{nj}, \end{aligned} \quad (2)$$

where the  $R'_j$  matrices define local rotation, which could be rewritten as two vectors  $\mathbf{u}_j$  and  $\mathbf{v}_j$ ,

$$\begin{aligned} \mathbf{u}_j &= R_j^{\alpha 1} + i R_j^{\alpha 2}, \\ \mathbf{v}_j &= R_j^{\alpha 3}, \end{aligned} \quad (3)$$

where  $\alpha 1, \dots, \alpha 3$  denote columns of the transformation matrices. The  $\mathbf{u}_j$  is the complex vector and  $\mathbf{v}_j$  is parallel to the selected spin vector in the rotating frame. These vectors, along with position of the moments, are shown in Table I.

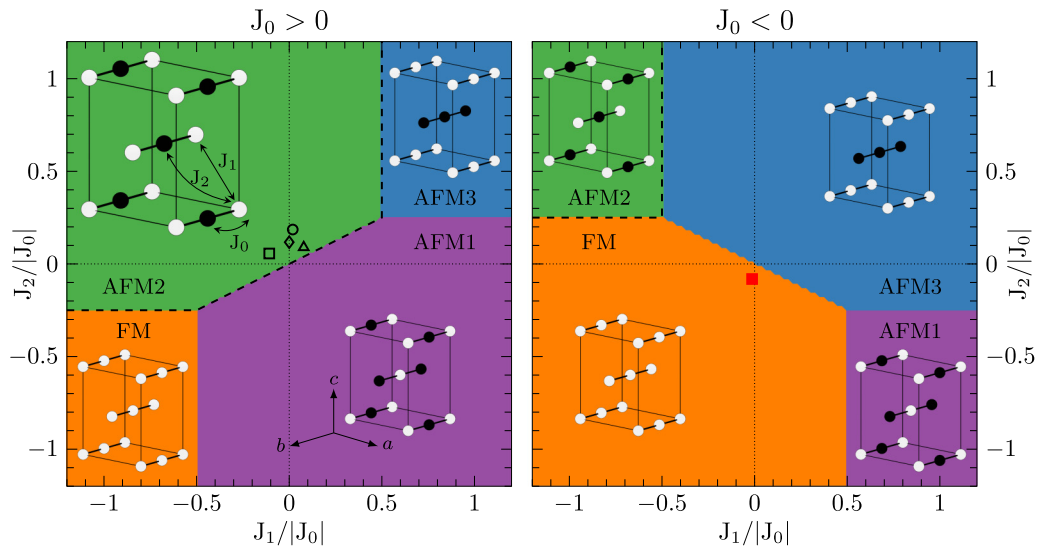


FIG. 2. Ground state magnetic phase diagrams as a function of interchain exchange interactions  $J_1$  and  $J_2$  normalized at the intrachain one,  $J_0$ , obtained through energy minimization (colored regions) and according to the real domain of Eq. (12) (thick dashed line). Black and white spheres depict opposite directions of magnetic moments. Left and right panels correspond to antiferromagnetic and ferromagnetic intrachain interaction, respectively. Insets depict structures with only magnetic ions shown. Marks show sets of exchange parameters for  $\text{PbFeBO}_4$  calculated in this work (square) and by Koo *et al.* [16] (circle), Xiong *et al.* [12] (triangle), Curti *et al.* (set b) [17] (diamond), and for  $\text{PbMnBO}_4$ , Koo *et al.* [16] (red square).

Next, the expansion of the Hamiltonian as a function of  $1/\sqrt{S}$  is achieved utilizing the Holstein-Primakoff approximation [24] to transform local spin operators in terms of the boson creation and annihilation operators  $b_i^\dagger$  and  $b_i$ . Keeping only the lowest order, the linear approximation is created:

$$\begin{aligned}\bar{S}_{nj}^{\prime\prime+} &= \sqrt{2S_j}b_{nj}, \\ \bar{S}_{nj}^{\prime\prime-} &= \sqrt{2S_j}b_{nj}^\dagger, \\ \bar{S}_{nj}^{\prime\prime z} &= S_j - b_{nj}^\dagger b_{nj},\end{aligned}\quad (4)$$

satisfying the following bosonic commutation relations,

$$[b_{mi}, b_{nj}^\dagger] = \delta_{mn}\delta_{ij}, \quad (5)$$

where  $m$  and  $n$  index the unit cell, while  $i$  and  $j$  index the magnetic moments within the cell ( $N = 4$ ).

With Fourier-transformed bosonic operators and spin operators in the rotating frame, the second-order term of Eq. (1) can be written in matrix form:

$$H_2 = \sum_{\mathbf{k} \in \text{B.Z.}} \mathbf{x}^\dagger(\mathbf{k}) \mathbf{h}(\mathbf{k}) \mathbf{x}(\mathbf{k}), \quad (6)$$

where  $\mathbf{x}$  is the vector of bosonic operators,

$$\mathbf{x} = [b_1(\mathbf{k}), \dots, b_4(\mathbf{k}), b_1^\dagger(-\mathbf{k}), \dots, b_4^\dagger(-\mathbf{k})]^\text{T}. \quad (7)$$

The commutation relation of these operators expressed in matrix form is the following:

$$[\mathbf{x}, \mathbf{x}^\dagger] = \mathbf{x}(\mathbf{x}^*)^\text{T} - (\mathbf{x}^* \mathbf{x}^\text{T})^\text{T} = \mathbf{g}, \quad (8)$$

where  $\mathbf{x}^*$  is the column matrix of the Hermitian adjoint operators. The commutator matrix has the following form:

$$\mathbf{g} = \begin{bmatrix} \mathbb{1} & 0 \\ 0 & -\mathbb{1} \end{bmatrix}, \quad (9)$$

where  $\mathbb{1}$  is an  $N \times N$  identity matrix.

Applying Fourier transformation of the exchange couplings, the quadratic form of the Hamiltonian is obtained:

$$\mathbf{h}(\mathbf{k}) = \begin{pmatrix} a & b^* & 0 & 0 & 0 & 0 & c^* & e^* \\ b & a & 0 & 0 & 0 & 0 & d & c^* \\ 0 & 0 & a & b^* & c & d^* & 0 & 0 \\ 0 & 0 & b & a & e & c & 0 & 0 \\ 0 & 0 & c^* & e^* & a & b^* & 0 & 0 \\ 0 & 0 & d & c^* & b & a & 0 & 0 \\ c & d^* & 0 & 0 & 0 & 0 & a & b^* \\ e & c & 0 & 0 & 0 & 0 & b & a \end{pmatrix}, \quad (10)$$

where

$$\begin{aligned}a &= 2S(-D + J_0 - 2J_1 + 4J_2), \\ b &= SJ_1(1 + e^{2\pi ih})(1 + e^{2\pi il}), \\ c &= SJ_0(1 + e^{2\pi ik}), \\ d &= 8SJ_2 \cos(\pi h) \cos(\pi k) \cos(\pi l) e^{\pi i(h-k+l)}, \\ e &= SJ_2(1 + e^{2\pi ih})(1 + e^{2\pi ik})(1 + e^{2\pi il}).\end{aligned}\quad (11)$$

Eigenvalues [25] of the  $\mathbf{gh}(\mathbf{k})$  lead to two positive (other  $N$  eigenvalues equivalent but negative) doubly degenerate, in the absence of external magnetic field, spin-wave modes corresponding to acoustical and optical

branches:

$$\begin{aligned}\omega &= 2S[(D - J_0 + 2J_1 - 4J_2)^2 \\ &\mp 4 \cos(\pi h) \cos(\pi l)(DJ_1 + 2J_1(J_1 - 2J_2) \\ &+ J_0(J_2 - J_1) + J_0J_2 \cos(2\pi k) \mp J_1^2 \cos(\pi h) \cos(\pi l)) \\ &- \cos^2(\pi k)(J_0^2 + 16J_2^2 \cos^2(\pi h) \cos^2(\pi l))]^{1/2},\end{aligned}\quad (12)$$

where  $h, k, l$  are given in reciprocal lattice units, and different branches are distinguished by the  $\mp$  sign. Obtained dispersion curves and reciprocal space surfaces are shown in Figs. 3 and 4, respectively.

All the calculations and plots were done with a small value of the uniform easy-axis type anisotropy ( $D$ ) of  $-0.01$  meV (along the  $c$  axis) to reproduce the observed magnetic structure of  $\text{PbFeBO}_4$  [10]. The specific symmetry of the  $Pnmm$  space group of  $\text{PbFeBO}_4$  leads to opposite tilting of  $[\text{FeO}_6]$  octahedra both within the chains as well as between them (as can be seen in Fig. 1), which could, potentially, lead to the site-dependent single-ion anisotropy, where the local anisotropy axis deviates from the  $c$  axis depending on the  $\text{Fe}^{3+}$  ion site. However, all experimental observations to date can be described with a uniform single-axis type of SIA, and it allows obtaining the closed-form solution for magnon frequencies, Eq. (12). It should also be noted that some part of the effects attributed to SIA could potentially arise from the small contribution of dipole-dipole interaction between nearest-neighbor moments within chains, which could be estimated as  $\approx 0.05$  meV assuming collinear moments and isotropic  $g$  factor. Despite the fact that it is impossible to derive the precise value of SIA based on the existing experimental data, which will require the frequency of the acoustical magnon, it is possible to estimate its boundaries. No acoustical modes were observed above  $10 \text{ cm}^{-1} \approx 1.24$  meV according to Ref. [15]; thus it can be used to estimate a higher boundary of SIA. The lower one could be estimated by taking into account the absence of acoustic mode up to  $140 \text{ GHz} \approx 4.17 \text{ cm}^{-1} \approx 0.58$  meV in antiferromagnetic resonance (AFMR) experiments [14]. Thus using the set of the exchange constants from Table II and with Eq. (12) will get anisotropy bounds of  $-0.015 < D < -0.0033$  meV. The validity of the obtained analytical results was confirmed by numerical calculations with the SpinW library [19,23].

### A. Two-magnon scattering

The most prominent feature observed in the magnetic Raman scattering spectra [15] below  $T_N$  is the broad and complex-shaped band attributed to the two-magnon scattering process due to its spectral and temperature-dependent characteristics. First, we will start with the selection rules. The effective two-magnon Raman Hamiltonian can be written according to the exchange scattering Fleury-Loudon mechanism [26]:

$$\mathcal{H}_R \propto \sum_{i,j} (\mathbf{e}_I \cdot \mathbf{d})(\mathbf{e}_S \cdot \mathbf{d}) \mathbf{S}_i \mathbf{S}_j, \quad (13)$$

where  $\mathbf{e}_I$  and  $\mathbf{e}_S$  denote the polarization vectors of the incident and scattered light, and  $\mathbf{d}$  is the vector connecting the  $i$ th ion with its nearest neighbor for the specific exchange coupling.

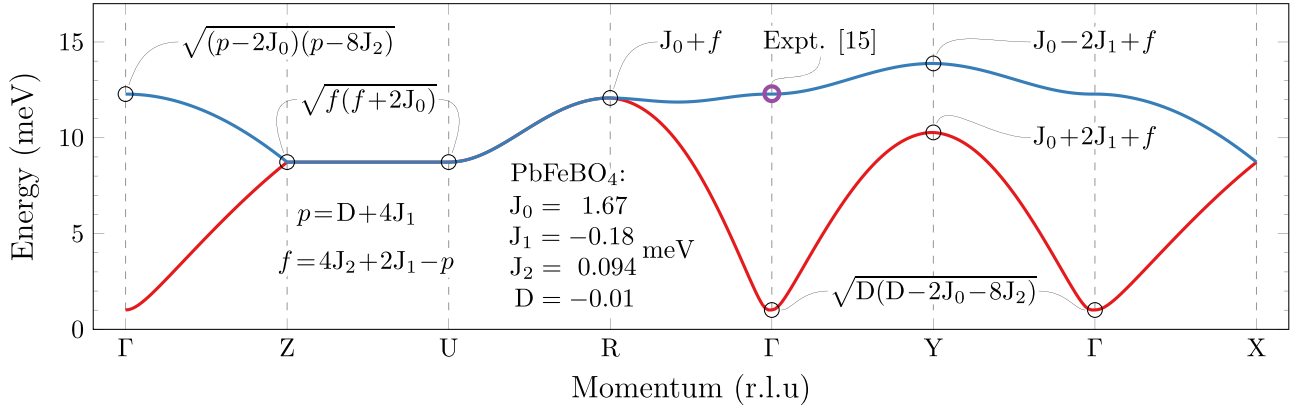


FIG. 3. Spin-wave dispersion along the high-symmetry path in the Brillouin zone according to Eq. (12). To obtain the energy of the highlighted points equations should be multiplied by  $2S$  (e.g.,  $S = 5/2$  for  $\text{PbFeBO}_4$ ). The purple circle shows the energy of the optical magnon branch observed in Raman scattering [15].

Thus, taking into account only the dominant intrachain  $J_0$  interaction, this analysis predicts nonzero two-magnon scattering intensity only in  $(bb)$  polarizations, the case where both incident and scattered light is polarized along the chains, which was, indeed, observed in the experiment [15].

It is known that two-magnon excitations observed, e.g., by Raman scattering reflect the spin-wave density of states (DOS) [26,27], which can be directly calculated based on dispersion relations in Eq. (12). It is necessary to use the full form of the Hamiltonian in Eq. (1) including all the exchange interactions to calculate the energy-dependent shape of the two-magnon band. The density of states is calculated according to

$$\text{DOS} = \oint_{\omega(\mathbf{k})=\epsilon} \frac{dS}{|\nabla\omega(\mathbf{k})|}, \quad (14)$$

where the integral is taken numerically through constant energy surfaces within the first Brillouin zone. The results of the calculations for different sets of exchange couplings from Table II in comparison with the experiment are shown in Fig. 5. Note how drastically the shape is affected by  $J_1$  and  $J_2$ , which allows us to undoubtedly determine them.

The possibility of calculating energy of the optical mode and one-magnon DOS opens a way to run an optimization

procedure to extract a representative set of the exchange constants. This procedure was implemented in two successive steps: The first step involves a rough grid search over the AFM2 domain depicted in Fig. 2 with the steps of 0.1 and 0.05 meV for  $J_0$ , and  $J_1$ ,  $J_2$ , respectively. This step was necessary to avoid local minima and for obtaining a good starting point for next minimization step. The second step involves numerical minimization of the  $F = A + B = (\text{OM}_{\text{expt}} - \text{OM}_{\text{calc}})^2 + \sum (2M - 2 \times \text{DOS})^2$  function, where  $\text{OM}_{\text{expt}}$  is the energy of the optical magnon branch observed in Raman scattering experiment, 12.4 meV [15],  $\text{OM}_{\text{calc}}$  is the energy of the same branch at the  $\Gamma$  point obtained from the calculated set,  $2M$  is the experimentally observed profile of the two-magnon excitation, and DOS is the calculated profile of the one-magnon DOS according to Eq. (14), shown in Fig. 5 as red circles and a purple shaded area, respectively. Note that multiplication by 2 is necessary to mimic the energy of the two-magnon scattering process. The summation was performed point by point in the ranges of 14–17 and 21–29 meV to exclude an intense phonon of the  $A_g$  symmetry.

This approach leads to an optimal set of the exchange constants  $J_0 = 1.67$ ,  $J_1 = -0.18$ , and  $J_2 = 0.094$  meV which allowed us to capture all essential experimental observations [15] such as (i) the high-energy cutoff of the band at 28 meV,

TABLE II. Comparison of the exchange constants (meV,  $J > 0$  corresponds to AFM) and derived parameters, such as energies of the optical magnon branch [OM, meV, calculated according to Eq. (12)], and Weiss temperatures  $\Theta_{\text{calc}}$  [K, calculated according to Eq. (15)].

	$J_0$	$J_1$	$J_2$	$\text{OM}_{\text{calc}}$	$\text{OM}_{\text{expt}}$	$\Theta_{\text{calc}}$	$\Theta_{\text{expt}}$
This work	1.67	-0.18	0.094	12.28		-228	
Koo <i>et al.</i> [16]	1.81	0.03447	0.3361	14.95		-436	
Xiang <i>et al.</i> [12]	2.321	0.1815	0.20775	9.64		-476	
Curti <i>et al.</i> [17] <sup>a</sup>	1.896	0.03447	0.259	13.35		-406	
Curti <i>et al.</i> [17] <sup>a</sup>	2.1285	0.0	0.2499	14.64		-423	
Pankrats <i>et al.</i> [14]							-263 <sup>b</sup>
Park <i>et al.</i> [10]	2.24			11.2		-303	
Prosnikov <i>et al.</i> [15]	2.23			11.15	12.4		

<sup>a</sup>For only electronic energy and additional terms, respectively. For details see Table 1 in Ref. [17].

<sup>b</sup>Averaged value, anisotropic ones are  $\Theta_a = -256$  K,  $\Theta_b = -272$  K, and  $\Theta_c = -262$  K [14].

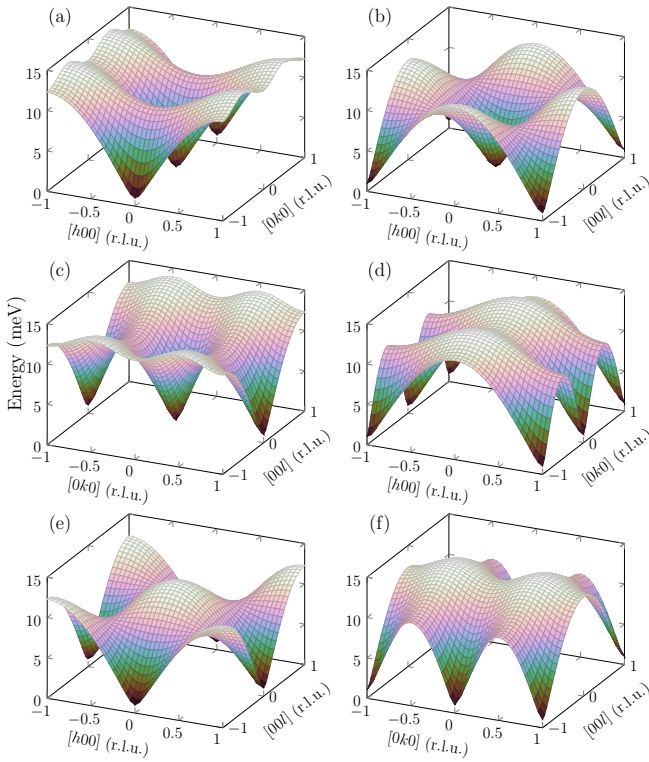


FIG. 4. (a–c) Acoustic and (d–f) optical branches of spin-wave dispersion for  $\text{PbFeBO}_4$  given by Eq. (12) with exchange coupling constants derived from Raman scattering experimental data ( $J_0 = 1.67$ ,  $J_1 = -0.18$ ,  $J_2 = 0.094$ ,  $D = -0.01$  meV).

(ii) the characteristic curvature of the band in the 24–28 meV range, (iii) the nearly linear DOS of maximal energy within 21–24 meV, and (iv) the nonzero and nonlinear low-energy tail for energies less than 17 meV.

The limiting factors of further refinement of the exchange constants using the 2M band are the presence of the intense phonon with the same  $A_g$  symmetry with the energy of  $\approx 19.5$  meV (thus, for the optimization procedure the region of 17–21 meV was excluded), overshadowing part of the expected singularities, a rather noisy Raman spectrum, and the absence of quantitative information on the lower energy tail. Moreover, the two-step procedure and constrained minimization do not allow to extract standard errors on the exchange couplings.

It should be noted that the one-magnon DOS surprisingly well describes the experimentally observed two-magnon band. Usually, it is apparently different due to the magnon-magnon interactions that strongly dampen and shift such excitations, and the trigonometric weighting factors [26] leading to band-shape deviations from the calculated DOS for different polarization configurations [27,28] which was demonstrated in paradigmatic examples of NiO [29] and  $\text{RbMnF}_3$  [30]. However, it seems both these contributions are insignificant for  $\text{PbFeBO}_4$ . The negligible role of the magnon-magnon interactions could mean an increased lifetime of spin excitations [31], which is a highly desirable goal for practical applications in antiferromagnetic spintronics [1]. An interesting aspect is the presence of the pronounced Van Hove singularities in the 2M band, which can provide access

to magnons in the specific points in the Brillouin zone and could be potentially applied to modulate exchange interactions and to control magnetic order in ultrafast timescales [32,33]. Another striking feature is the accidental degeneracy of the high-energy (12.4-meV) optical magnon branch with  $A_g$  phonon in the low-temperature limit, which could be used for spin dynamics manipulation through optical phonon pumping [34].

## B. Comparison with *ab initio* calculations

Realization of both ferromagnetic and antiferromagnetic structures for different magnetic ions without change of the crystal symmetry in the  $\text{Pb}M\text{BO}_4$  ( $M = \text{Cr}, \text{Mn}, \text{Fe}$ ) family sparked the interest, and a few computational works [12,16,17] were done to shed light on this phenomenon. Lattice dynamics was addressed in Refs. [13,17] and, in general, shows a good match with experimental data both on powdered samples [13] and single crystals [15].

Exchange constants up to the third nearest neighbor were directly calculated in Refs. [16,17] and, using an energy mapping analysis (Eq. (3) in Ref. [16]), it is possible to extract constants from the energies of the magnetic structures from Ref. [12], which are all summarized in Table II and graphically shown in Fig. 2. All calculations agree on the dominant role of the intrachain exchange ( $J_0$ ). The  $J_1$  is either antiferromagnetic or zero in the case of Gibbs free energy calculations [17] and smaller than  $J_2$ , which is also antiferromagnetic. It was shown that exchange constants are strongly dependent on the Hubbard parameter  $U$  in the DFT +  $U$  scheme [16]. The comparison of the sets with the experimental 2M band presented in Fig. 5 clearly shows interchain coupling sensitivity, and substantial deviation for all the *ab initio* sets.

Besides the direct determination of the exchange constants based on one- and two-magnon excitations, it is possible to use static magnetic data as an additional consistency check. For example, Curie-Weiss temperature (sometimes referred to as Weiss or paramagnetic Curie temperature), which is the arithmetic average of all the exchange constants in the system [35], could be used. Taking into account the number and symmetry of the exchange couplings, it can be calculated as

$$\Theta = -\frac{2}{3}S(S+1)[2J_0 + 4J_1 + 8J_2]/k_B. \quad (15)$$

This parameter could be experimentally determined from the temperature dependence of the magnetic susceptibility for  $T > T_N$ . This was done experimentally [14], and the reported values are negative, suggesting predominantly antiferromagnetic interactions in the system, and slightly anisotropic  $\Theta_a = -256$ ,  $\Theta_b = -272$ , and  $\Theta_c = -262$  K. Most of the sets, proposed in *ab initio* works [12,16,17], overestimate  $\Theta$  by 54–81%. In contrast the optimal set of the exchange constants results in a much closer value of  $\Theta = -228$  K. The deviation of  $\Theta$  from the proposed set could be explained by additional unaccounted superexchange couplings beyond  $J_2$  or by the contribution of nonisotropic exchange interactions (see Sec. II C).

However, it should be noted that for decisive Curie-Weiss analysis the temperature range above the transition should be typically five to ten times larger than the Weiss temperature itself [36], which is not the case for  $\text{PbFeBO}_4$ , since it has

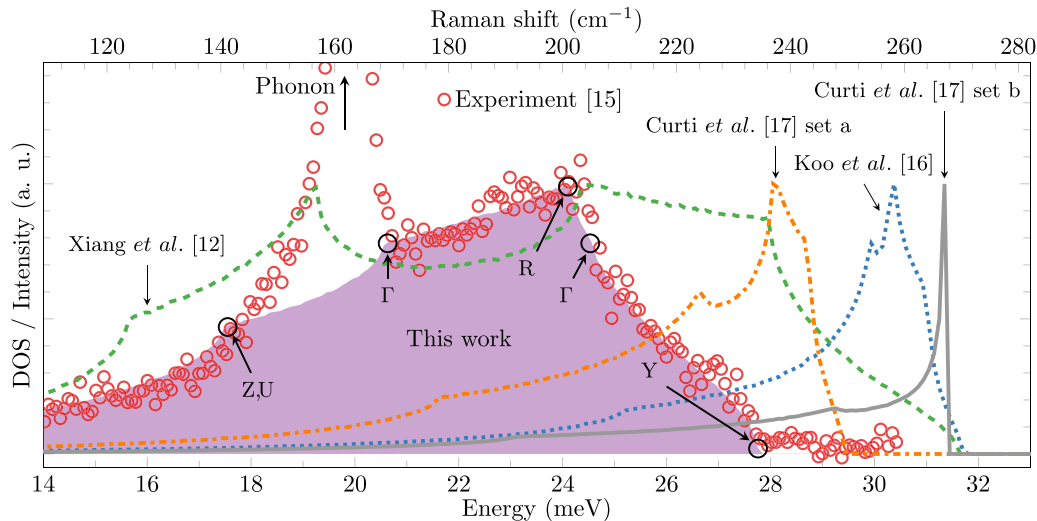


FIG. 5. Comparison of experimental Raman scattering spectra of the two-magnon band (red marks, data extracted from Fig. 5 in Ref. [15]) with the spin-wave density of states calculated according to Eq. (14) with exchange constants from this work (purple shaded area) and Refs. [12,16,17], (see Table II). Note that the DOS energy scale is doubled to match the 2M excitation. Arrows indicate Van Hove singularities in the DOS with corresponding critical points in the Brillouin zone, which can be seen in Fig. 3.

both high  $T_N = 114$  K and  $\Theta = -263$  K, while in experiment magnetic susceptibility was measured only up to 300 K.

The calculated exchange parameters in comparison with previously suggested ones are summarized in Table II. We hope that the proposed set of exchange constants, compatible with all experimental observations to date, will be used for a systematic search of the  $U$  parameter in such a challenging system as  $\text{PbFeBO}_4$ .

### C. Beyond isotropic exchange

The unexplained anomaly was reported in Ref. [14], where, unusual for a typical easy-axis antiferromagnet, a peaklike maximum in the magnetic susceptibility for  $H \parallel b$  geometry was measured. Thus the potential presence of the anisotropic exchange coupling terms, such as the Dzyaloshinskii-Moriya interaction, should be discussed. In most cases, such interaction leads to a spin canting resulting in similar anomalies in susceptibility and a presence of the weak macroscopic magnetic moment in antiferromagnets [37,38], like in some well-known cases such as  $\text{FeBO}_3$  [39],  $\text{LiCoPO}_4$  [40], and perovskite manganites [41]. However, no magnetic moment was registered in  $\text{PbFeBO}_4$  for all the available field ranges and geometries [14].

It is known that DMI is governed by lattice symmetry [37]. Due to the presence of a mirror plane ( $m$ ) perpendicular to the  $J_0$  exchange path and passing through its center, only  $[\text{DM}_x, 0, \text{DM}_z]$  components of the DMI vector are allowed. The  $\text{DM}_x$  will lead to a slight canting of the spins within  $bc$  planes inducing a small ferromagnetic moment along individual chains. However, due to the symmetry of the lattice, this canting is compensated by the same moment with the opposite direction from neighboring chains. This canting is fully compatible with the previously suggested magnetic space group  $Pnma$  [15] and can be described with a  $\Psi_x$  basis function. On

the other hand, the contribution of the  $\text{DM}_z$  is negligible due to the orientation of the magnetic moments along the same axis.

Thus, the contribution of the antisymmetric exchange interaction with the  $\text{DM}_x$  component can simultaneously explain the kinklike anomaly in magnetic susceptibility for  $H \parallel b$  at  $T_N$  and the absence of weak ferromagnetic moment at lower temperatures. This interaction will also directly affect spin dynamics in the form of magnon degeneracy lifting even without an external magnetic field presence. Numerical estimation of the acoustic mode splitting by the DMI with the semiarbitrary value of 0.167 meV (1/10 of  $J_0$ ) leads to  $2.46 \text{ cm}^{-1} \approx 0.3 \text{ meV}$  splitting of the acoustic mode which should be experimentally detectable with reasonably high-resolution Raman or IR spectroscopy setups.

### D. Magnetic structure dimensionality

The assumption of the (quasi-)one-dimensional (1D) magnetism in  $\text{PbFeBO}_4$  comes naturally considering its crystal structure, consistent with the well-separated chains of  $[\text{FeO}_6]$  octahedra running along the  $b$  axis [10]. The broad features above  $T_N$  in dc magnetic susceptibility on powdered samples [10] was also considered as a manifestation of short-range ordering characteristic for low-dimensional magnetic systems. However, the detailed susceptibility investigation on the high-quality single crystals [14] showed that broad features were caused by  $\alpha\text{-Fe}_2\text{O}_3$  contamination, and  $\chi$  behaves closer to a three-dimensional Heisenberg antiferromagnet (except for the kink anomaly which was discussed in Sec. II C).

As the magnetic dimensionality measure, ratios of the intra- to interchain exchange couplings, taking into account coordination number ( $z_n$ ), could be used [42]. The set of the optimal constants gives the following values: 1:0.22:0.22 of  $|J_0| * z_0 : |J_1| * z_1 : |J_2| * z_2$ , which is closer to a 3D case, in comparison with other well-known one-dimensional systems

such as as TTF-CuBDT [43], CuGeO<sub>3</sub> [44], and KCuF<sub>3</sub> [45] with ratios  $J_{\text{intra}}/J_{\text{inter}} \ll 1$ . Moreover, in most 1D systems, only single, nearest-neighbor (NN) interchain coupling is considered important to capture spin dynamics properties, while for PbFeBO<sub>4</sub>, all interactions up to third-nearest neighbor (NN, NNN, and NNNN) couplings are essential.

Thus, based on the above, PbFeBO<sub>4</sub> should be considered a three-dimensional antiferromagnet in the low-temperature limit  $T \ll T_N$ . However, according to the magnetic susceptibility anomaly observed in Ref. [14] and intense magnetic quasielastic scattering observed in polarization along the chains [15], there is a possibility of quasi-one-dimensional behavior manifestation in the vicinity of the phase transition. Another possibility could lie in the domain of the reduced dimensionality due to frustrations as was demonstrated in layered anisotropic triangular-lattice Heisenberg antiferromagnets Cs<sub>2</sub>CuCl<sub>4-x</sub>Br<sub>x</sub> [46].

### E. Spin dynamics of PbCrBO<sub>4</sub>

In comparison with PbFeBO<sub>4</sub>, the magnetic structure of PbCrBO<sub>4</sub> differs only in the direction of the easy axis [10]; thus, all previously derived equations and conclusions could be directly applied for an estimation of the energy of one- and two-magnon excitations. Considering more than one order of magnitude lower,  $T_N = 8$  K, and  $\Theta = 45$  K, the exchange constants are expected to be proportionally smaller. However, up to now, there are no published data on the spin dynamics of PbCrBO<sub>4</sub>.

According to Ref. [16] the exchange parameters of the optimized structure (calculated with Hubbard parameter  $U = 2.0$  eV) are  $J_0 \approx 0.52$  meV,  $J_1 \approx -0.0345$  meV, and  $J_2 \approx 0.069$  meV, which with the reduced, in comparison with PbFeBO<sub>4</sub>, spin value of Cr<sup>3+</sup> ions  $S = 3/2$  gives the expected energy of the two-magnon excitation band maximum of  $\approx 5$  meV and the energy of the optical magnon mode at  $\approx 2.7$  meV, which are both accessible in typical low-energy Raman scattering experiments.

### III. SUMMARY AND CONCLUSION

With the use of linear spin-wave theory, the closed form of the magnon dispersion relation of PbFeBO<sub>4</sub> was derived, including exchange couplings up to the third nearest neighbor and single-ion anisotropy of the easy-axis type. It is demonstrated that magnetic excitations observed in Raman scattering [15] are optical (exchange) magnon and two-magnon band and, based on their energy and magnetic susceptibility data [14], the following consistent set of exchange coupling constants is proposed:  $J_0 = 1.67$ ,  $J_1 = -0.18$ , and  $J_2 = 0.094$  meV. It is shown that *ab initio* calculations [12,16,17] overestimate both  $J_0$  and  $J_2$  while predicting the opposite sign for  $J_1$ . Nonzero components of the Dzyaloshinskii-Moriya interaction are allowed for the  $J_0$  exchange path, which could be responsible for the magnetic susceptibility anomaly [14]. Surprisingly, the shape of the two-magnon band is well described by the one-magnon density of states, which indicates a vanishingly small role of the magnon-magnon interactions. We hope that the obtained results will stimulate both experimental research, such as IR and low-energy Raman spectroscopy to find acoustic modes and inelastic neutron scattering to directly probe magnon dispersion, and high-temperature magnetic susceptibility for accurate determination of Weiss temperatures, and theoretical ones on spin dynamics and a systematic study of the exchange coupling constants' dependence on the Hubbard parameter ( $U$ ) for *ab initio* calculations.

### ACKNOWLEDGMENTS

The support of R. V. Pisarev, A. M. Kalashnikova, and A. V. Azovtsev, fruitful discussions with Beatrice T. Crow, and assistance with the carbon tube by M. Berben are greatly acknowledged. We also acknowledge the support of the HFML-RU/NWO-I, member of the European Magnetic Field Laboratory (EMFL).

- 
- [1] P. Němec, M. Fiebig, T. Kampfrath, and A. V. Kimel, Antiferromagnetic opto-spintronics, *Nat. Phys.* **14**, 229 (2018).
  - [2] E. V. Gomonay and V. M. Loktev, Spintronics of antiferromagnetic systems, *Low Temp. Phys.* **40**, 17 (2014).
  - [3] V. Baltz, A. Manchon, M. Tsoi, T. Moriyama, T. Ono, and Y. Tserkovnyak, Antiferromagnetic spintronics, *Rev. Mod. Phys.* **90**, 015005 (2018).
  - [4] T. Jungwirth, X. Marti, P. Wadley, and J. Wunderlich, Antiferromagnetic spintronics, *Nat. Nanotechnol.* **11**, 231 (2016).
  - [5] N. A. Spaldin and R. Ramesh, Advances in magnetoelectric multiferroics, *Nat. Mater.* **18**, 203 (2019).
  - [6] J. Son, B. C. Park, C. H. Kim, H. Cho, S. Y. Kim, L. J. Sandilands, C. Sohn, J.-G. Park, S. J. Moon, and T. W. Noh, Unconventional spin-phonon coupling via the Dzyaloshinskii-Moriya interaction, *npj Quantum Mater.* **4**, 17 (2019).
  - [7] S. Han, J. Lee, and E.-G. Moon, Lattice vibration as a knob on exotic quantum criticality, *Phys. Rev. B* **103**, 014435 (2021).
  - [8] R. X. Fischer and H. Schneider, Crystal chemistry of borates and borosilicates with mullite-type structures: A review, *Eur. J. Mineral.* **20**, 917 (2008).
  - [9] M. M. Murshed, R. X. Fischer, and T. M. Gesing, The role of the Pb<sup>2+</sup> lone electron pair for bond valence sum analysis in mullite-type PbMBO<sub>4</sub> (M = Al, Mn and Fe) compounds, *Z. Kristallogr. Cryst. Mater.* **227**, 580 (2012).
  - [10] H. Park, R. Lam, J. E. Greedan, and J. Barbier, Synthesis, crystal structure, crystal chemistry, and magnetic properties of PbMBO<sub>4</sub> (M = Cr, Mn, Fe): A new structure type exhibiting one-dimensional magnetism, *Chem. Mater.* **15**, 1703 (2003).
  - [11] A. Pankrats, K. Sablina, M. Eremin, A. Balaev, M. Kolkov, V. Tugarinov, and A. Bovina, Ferromagnetism and strong magnetic anisotropy of the PbMnBO<sub>4</sub> orthoborate single crystals, *J. Magn. Magn. Mater.* **414**, 82 (2016).
  - [12] H. Xiang, Y. Tang, S. Zhang, and Z. He, Intra-chain superexchange couplings in quasi-1D 3d transition-metal magnetic compounds, *J. Phys.: Condens. Matter* **28**, 276003 (2016).

- [13] M. M. Murshed, C. B. Mendive, M. Curti, G. Nénert, P. E. Kalita, K. Lipinska, A. L. Cornelius, A. Huq, and T. M. Gesing, Anisotropic lattice thermal expansion of  $\text{PbFeBO}_4$ : A study by x-ray and neutron diffraction, Raman spectroscopy and DFT calculations, *Mater. Res. Bull.* **59**, 170 (2014).
- [14] A. Pankrats, K. Sablina, D. Velikanov, A. Vorotynov, O. Bayukov, A. Eremin, M. Molokeev, S. Popkov, and A. Krasikov, Magnetic and dielectric properties of the  $\text{PbFeBO}_4$  single crystal, *J. Magn. Magn. Mater.* **353**, 23 (2014).
- [15] M. A. Prosnikov, A. N. Smirnov, V. Y. Davydov, K. A. Sablina, and R. V. Pisarev, Lattice and magnetic dynamics of a quasi-one-dimensional chain antiferromagnet  $\text{PbFeBO}_4$ , *J. Phys.: Condens. Matter* **29**, 025808 (2016).
- [16] H.-J. Koo and M.-H. Whangbo, Density functional investigation of the magnetic properties of  $\text{PbMBO}_4$  ( $M = \text{Cr, Mn, Fe}$ ), *Solid State Commun.* **149**, 602 (2009).
- [17] M. Curti, M. M. Murshed, T. Bredow, D. W. Bahnemann, T. M. Gesing, and C. B. Mendive, Elastic, phononic, magnetic and electronic properties of quasi-one-dimensional  $\text{PbFeBO}_4$ , *J. Mater. Sci.* **54**, 13579 (2019).
- [18] M. Curti, C. B. Mendive, T. Bredow, M. M. Murshed, and T. M. Gesing, Structural, vibrational and electronic properties of  $\text{SnMBO}_4$  ( $M = \text{Al, Ga}$ ): A predictive hybrid DFT study, *J. Phys.: Condens. Matter* **31**, 345701 (2019).
- [19] S. Tóth, tsdev/spinw: pypinw 3.0, 2017, DOI:10.5281/zenodo.838034.
- [20] D. Beeman and P. Pincus, Nuclear spin-lattice relaxation in magnetic insulators, *Phys. Rev.* **166**, 359 (1968).
- [21] R. S. Fishman, J. A. Fernandez-Baca, and T. Rößler, in *Spin-Wave Theory and its Applications to Neutron Scattering and THz Spectroscopy* (Morgan and Claypool, San Rafael, CA, 2018).
- [22] S. Petit, Numerical simulations and magnetism, *École thématique de la Société Française de la Neutronique* **12**, 105 (2011).
- [23] S. Toth and B. Lake, Linear spin wave theory for single-Q incommensurate magnetic structures, *J. Phys.: Condens. Matter* **27**, 166002 (2015).
- [24] T. Holstein and H. Primakoff, Field dependence of the intrinsic domain magnetization of a ferromagnet, *Phys. Rev.* **58**, 1098 (1940).
- [25] R. M. White, M. Sparks, and I. Ortenburger, Diagonalization of the antiferromagnetic magnon-phonon interaction, *Phys. Rev.* **139**, A450 (1965).
- [26] P. A. Fleury and R. Loudon, Scattering of light by one- and two-magnon excitations, *Phys. Rev.* **166**, 514 (1968).
- [27] R. W. Davies, S. R. Chinn, and H. J. Zeiger, Spin-wave approach to two-magnon Raman scattering in a simple antiferromagnet, *Phys. Rev. B* **4**, 992 (1971).
- [28] R. J. Elliott and M. F. Thorpe, The effects of magnon-magnon interaction on the two-magnon spectra of antiferromagnets, *J. Phys. C* **2**, 1630 (1969).
- [29] R. E. Dietz, G. I. Parisot, and A. E. Meixner, Infrared absorption and Raman scattering by two-magnon processes in  $\text{NiO}$ , *Phys. Rev. B* **4**, 2302 (1971).
- [30] P. A. Fleury, Evidence for Magnon-Magnon Interactions in  $\text{RbMnF}_3$ , *Phys. Rev. Lett.* **21**, 151 (1968).
- [31] M. E. Zhitomirsky and A. L. Chernyshev, Colloquium: Spontaneous magnon decays, *Rev. Mod. Phys.* **85**, 219 (2013).
- [32] J. H. Mentink, Manipulating magnetism by ultrafast control of the exchange interaction, *J. Phys.: Condens. Matter* **29**, 453001 (2017).
- [33] G. Batignani, D. Bossini, N. Di Palo, C. Ferrante, E. Pontecorvo, G. Cerullo, A. Kimel, and T. Scopigno, Probing ultrafast photo-induced dynamics of the exchange energy in a Heisenberg antiferromagnet, *Nat. Photonics* **9**, 506 (2015).
- [34] T. F. Nova, A. Cartella, A. Cantaluppi, M. Först, D. Bossini, R. V. Mikhaylovskiy, A. V. Kimel, R. Merlin, and A. Cavalleri, An effective magnetic field from optically driven phonons, *Nat. Phys.* **13**, 132 (2017).
- [35] A. Czachor, Paramagnetic Curie temperature is an arithmetic average of the interspin coupling constants, *J. Magn. Magn. Mater.* **139**, 355 (1995).
- [36] R. R. P. Singh and J. Oitmaa, High-temperature thermodynamics of the honeycomb-lattice Kitaev-Heisenberg model: A high-temperature series expansion study, *Phys. Rev. B* **96**, 144414 (2017).
- [37] T. Moriya, Anisotropic superexchange interaction and weak ferromagnetism, *Phys. Rev.* **120**, 91 (1960).
- [38] A. Moskvina, Dzyaloshinskii-Moriya coupling in 3d insulators, *Condens. Matter* **4**, 84 (2019).
- [39] V. E. Dmitrienko, E. N. Ovchinnikova, S. P. Collins, G. Nisbet, G. Beutier, Y. O. Kvashnin, V. V. Mazurenko, A. I. Lichtenstein, and M. I. Katsnelson, Measuring the Dzyaloshinskii-Moriya interaction in a weak ferromagnet, *Nat. Phys.* **10**, 202 (2014).
- [40] E. Fogh, O. Zaharko, J. Schefer, C. Niedermayer, S. Holm-Dahlin, M. K. Sørensen, A. B. Kristensen, N. H. Andersen, D. Vaknin, N. B. Christensen, and R. Toft-Petersen, Dzyaloshinskii-Moriya interaction and the magnetic ground state in magnetoelectric  $\text{LiCoPO}_4$ , *Phys. Rev. B* **99**, 104421 (2019).
- [41] I. A. Sergienko and E. Dagotto, Role of the Dzyaloshinskii-Moriya interaction in multiferroic perovskites, *Phys. Rev. B* **73**, 094434 (2006).
- [42] P. Lemmens, G. Güntherodt, and C. Gros, Magnetic light scattering in low-dimensional quantum spin systems, *Phys. Rep.* **375**, 1 (2003).
- [43] C. Jeandey and M. Nechtschein, Inter- and intra-chain couplings in TTF  $\text{CuBDT}$  as determined from proton spin lattice relaxation time measurements, *J. Magn. Magn. Mater.* **15–18**, 1053 (1980).
- [44] M. Nishi, O. Fujita, and J. Akimitsu, Neutron-scattering study on the spin-Peierls transition in a quasi-one-dimensional magnet  $\text{CuGeO}_3$ , *Phys. Rev. B* **50**, 6508 (1994).
- [45] K. Hirakawa and Y. Kurogi, One-dimensional antiferromagnetic properties of  $\text{KCuF}_3$ , *Prog. Theor. Phys. Suppl.* **46**, 147 (1970).
- [46] U. Tutsch, O. Tsypliyatsev, M. Kuhnt, L. Postulka, B. Wolf, P. T. Cong, F. Ritter, C. Krellner, W. Abmus, B. Schmidt, P. Thalmeier, P. Kopietz, and M. Lang, Specific Heat Study of 1D and 2D Excitations in the Layered Frustrated Quantum Antiferromagnets  $\text{Cs}_2\text{CuCl}_{4-x}\text{Br}_x$ , *Phys. Rev. Lett.* **123**, 147202 (2019).